ROYAL SOCIETY
OF CHEMISTRY

PAPER

Check for updates

Ni/Ce$_{0.8}$Zr$_{0.2}$O$_{2-x}$ solid solution catalyst: a pathway to coke-resistant CO$_2$ reforming of methane†

Rubina Khatun,[a] Rohan Singh Pal,[a] Kapil Bhati,[a] Anil Chandra Kothari,[ab] Shivani Singh,[ab] Nazia Siddiqui,[a] Swati Rana[a] and Rajaram Bal [ID] ⋆[ab]

The CO$_2$ reforming of methane effectively produces syngas using two prevalent greenhouse gases: CO$_2$ and CH$_4$. This study investigates the performance of three nickel-based catalysts, Ni/ZrO$_2$, Ni/CeO$_2$ and Ni/Ce$_{0.8}$Zr$_{0.2}$O$_{2-x}$, in the DRM reaction. Each catalyst was thoroughly examined using a range of techniques, including XRD, TPR, BET, TPD, HR-TEM, Raman, O$_2$-TPD, XPS, TGA and CO$_2$-TPD to assess its structural and catalytic properties. The Ni/Ce$_{0.8}$Zr$_{0.2}$O$_{2-x}$ catalyst, combining the advantages of both supports to form a solid solution, achieved the best overall performance with enhanced activity and stability. Meanwhile, Ni/ZrO$_2$ and Ni/CeO$_2$ catalysts showed a tendency towards deactivation over extended reaction times. Characterization showed that incorporating zirconia into the CeO$_2$ lattice led to the solid solution synthesis with a solely defective cubic fluorite phase, as confirmed by XRD and Raman analysis. The TPR and CO$_2$-TPD revealed that the resulting Ni/Ce$_{0.8}$Zr$_{0.2}$O$_{2-x}$ catalyst possesses strong metal–support interaction and higher CO$_2$ adsorption compared to pure CeO$_2$ and ZrO$_2$ samples. This composite support facilitated the generation of oxygen vacancies/active oxygen species, which are beneficial for reducing coke deposition. The Ni/Ce$_{0.8}$Zr$_{0.2}$O$_{2-x}$ catalyst demonstrated exceptional performance, achieving around 90.8% methane conversion and 91.0% CO$_2$ conversion at 700 °C, with the resulting H$_2$/CO ratio precisely equal to one. The stability test revealed remarkable stability against coke deposition for Ni/Ce$_{0.8}$Zr$_{0.2}$O$_{2-x}$; meanwhile, Ni/ZrO$_2$ and Ni/CeO$_2$ are more susceptible to coke deposition, with the Ni/ZrO$_2$ sample showing a greater tendency towards graphitic coke deposition. This study highlights the importance of catalyst supports in optimizing the performance of nickel-based catalysts for CO$_2$ reforming applications.

Sustainability spotlight

The continuous increase in greenhouse gases, particularly carbon dioxide (CO$_2$) and methane (CH$_4$), has intensified global climate challenges. The CO$_2$ reforming reaction is particularly important for mitigating climate change, as it converts CO$_2$, a major greenhouse gas, into valuable products while also tackling the issue of methane emissions. DRM also offers a dual-purpose solution by converting the two harmful gases into syngas, a valuable mixture of hydrogen and carbon monoxide and closes the loop on carbon emissions, turning pollutants into resources. This process reduces the levels of these potent greenhouse gases and provides an efficient pathway to produce cleaner fuels and chemicals. This process aligns with several UN SDGs, including SDG 7, SDG 9, and SDG 13, contributing to a more sustainable and circular economy.

Introduction

CO$_2$ reforming/dry reforming of methane (DRM) has emerged as a pivotal reaction for the simultaneous production of H$_2$ and CO (syngas). This process not only provides a means to utilize greenhouse gases but also contributes to the production of essential chemicals and fuels.[1,2] The reaction is particularly significant for mitigating climate change by transforming CO$_2$, a major greenhouse gas, into useful products while simultaneously addressing the challenge of methane emissions.[3–5] Although, DRM offers benefits in terms of the environment and economy, a lack of highly active and coke-resistant catalysts hinders its commercial implementation on a large scale.[6,7] Several catalysts have been developed to tackle this obstacle.[4,8–10] Precious metals (Pt, Rh, Ru and Ir) are too expensive to be used widely due to their high cost. Ni-based catalysts are considered good substitutes due to their low cost and great capacity to activate C–H bonds.[11,12] However, the strong endothermic characteristics of DRM involve a high temperature for the reaction, which is associated with the

[a]Light Stock Processing Division, CSIR-Indian Institute of Petroleum, Dehradun 248005, India. E-mail: raja@iip.res.in; Fax: +91 135 2660202; Tel: +91 135 2525917
[b]Academy of Scientific and Innovative Research, Ghaziabad, Uttar Pradesh-201002, India

critical disadvantages of carbon deposition and sintering, issues that Ni-based catalysts encounter.[13–15]

Creating a reliable Ni-based catalyst for real-world industrial applications is essential. This process may require fine-tuning of several aspects, including the dispersion of active metal, the interactions between the metal and its support, the size of particles, the production of reactive oxygen species through defect formation, and the choice of suitable active metals, promoters and supports.[10,16] The uniform dispersion of active sites across the catalyst surface has been demonstrated to reduce coking by eliminating faceted Ni surfaces.[17–20] S. Ali and their group found that Ni/alumina catalysts prepared via the combustion method demonstrated significantly less coking compared to impregnated catalysts.[21] The high dispersion of Ni^0 species on the Ni/CeZrAl catalyst, combined with abundant oxygen vacancies and basic sites, promoted disordered carbon formation while protecting Ni active sites.[22] MV Grabchenko and their group found that the Ni/CeMnO$_x$/SBA-15 catalyst reduces coke formation compared to unmodified Ni/SBA-15, because of the high amount of reactive superoxo (O_2^-) and peroxo (O^-) species.[23]

The catalyst's effectiveness was attributed to its enhanced oxygen vacancies and strong metal–support interactions. The Ga-doped Ni/CeO$_2$ catalyst enhances CO$_2$ adsorption and activation, generating sufficient oxygen species to prevent carbon deposition and maintain catalytic activity, leading to superior stability and performance.[24] The defect-rich Pt–Ni/CeO$_2$ catalyst in DRM features abundant oxygen vacancies (O_V), facilitating CO$_2$ adsorption and its simultaneous dissociation into CO and O*. This mechanism contributes to the catalyst's exceptional stability against coke deposition.[16] The development of more facile oxygen vacancies (O_V) in the defect-rich Pt/CeO$_2$ catalyst accelerates DRM at low-temperatures, as observed by Shen et al.[25] R. Babakouhi et al. recently observed that adding 10 wt% CeO$_2$ markedly enhanced nickel dispersion and strengthened the interaction with the support.[26]

For DRM, numerous supports are employed, including CeO$_2$, ZrO$_2$, La$_2$O$_3$, MgO, TiO$_2$, SiC, boron nitride (BN), Al$_2$O$_3$, SiO$_2$, zeolite and metal–organic frameworks (MOFs).[27] Each support offers distinct chemical properties: CeO$_2$ is recognized for its exceptional ability to store oxygen; La$_2$O$_3$ and TiO$_2$ are recognized for their oxygen mobility; ZrO$_2$ and BN provide exceptional thermal stability.[27–31] These properties collectively contribute to the reduction of carbon deposition.[27] Coke formation is also minimized on materials with high oxygen storage capacities (OSCs) due to interactions between lattice oxygen and adsorbed carbon species.[32] The oxygen vacancies (O_V) in CeO$_2$ are generated by reducing Ce^{4+} to Ce^{3+} and can be replenished by dissociating CO$_2$, which helps prevent coke deposition and extend the catalyst's lifespan during DRM.[16,33] Ceria readily integrates with transition metals and other rare-earth elements to form solid solutions. The introduction of smaller cations (e.g., Si^{4+} and Zr^{4+}) and lower valence metal ions (e.g., Ni^{2+} and Sm^{3+}) into the ceria lattice creates additional O_V through lattice distortion, enhancing oxygen ion mobility and improving low-temperature catalytic activity.[2,16,34]

Ceria's high oxygen storage capacity (OSC) allows it to release and re-oxidize oxygen efficiently but this capacity decreases at elevated temperatures and under reductive conditions. At the same time, zirconium stabilizes ceria by creating a CeO$_2$–ZrO$_2$ solid solution that enhances its thermal resistance, catalytic activity and OSC.[35,36] Zr^{4+} doping into ceria generates structural distortions and defects that enhance its catalytic performance, with CeO$_2$–ZrO$_2$ composites being particularly effective as three-way catalysts.[32,36] The oxygen volume diffusion coefficient of this support is generally double that of pure ceria.[37] The Ni/CeO$_2$–ZrO$_2$ (Ni–CZ) catalyst synthesized via a one-pot procedure enhances Ni–CZ interaction, yielding smaller Ni nanoparticles, high dispersion and abundant oxygen vacancies, which promote coke gasification on the Ni surface.[38] High concentrations of Zr lead to a transformation from the fluorite structure to a tetragonal phase, which decreases the oxygen storage capacity (OSC) of the support.[39] Enhanced anti-sintering properties, excellent oxygen storage capacity, and strong thermal stability make CeO$_2$–ZrO$_2$ solid solutions a promising support material that has garnered significant attention.[18,32,40–42]

Herein, we aim to create a composite material that not only retains a sufficient level of oxygen storage but also significantly improves thermal stability. In this study, we demonstrate a novel and straightforward one-pot complex combustion method, utilizing citric acid, to synthesize a distorted cubic fluorite phase of the Ni/Ce$_{0.8}$Zr$_{0.2}$ solid solution catalyst with increased oxygen vacancies. This combination not only facilitates efficient methane activation and CO$_2$ conversion but also addresses issues related to catalyst deactivation, making it a valuable component in advancing DRM technology for sustainable energy solutions. Ni/CeO$_2$ and Ni/ZrO$_2$ catalysts were also synthesized using a similar method for comparable activity towards DRM.

Experimental

Catalyst preparation

The Ni/ZrO$_2$, Ni/CeO$_2$ and Ni/CeO$_2$–ZrO$_2$ catalysts were prepared using a straightforward one-pot complex combustion method. Specifications of the materials employed and the detailed synthesis procedure can be found in the ESI (S1.1 and S1.2).† The final catalysts, Ni/ZrO$_2$, Ni/CeO$_2$ and Ni/Ce$_{0.8}$Zr$_{0.2}$O$_{2-x}$, with 5 wt% Ni loading were designated as 5NZ, 5NC and 5NCZ, respectively. We also prepared 2.5 and 7.5 wt% Ni/Ce$_{0.8}$Zr$_{0.2}$O$_{2-x}$ catalysts to optimize the nickel loading for DRM, designated as 2.5NCZ and 7.5NCZ, respectively.

Catalyst characterization

The synthesized catalysts have been extensively analyzed using a variety of techniques. These included powder X-ray diffraction (XRD) for structural analysis, surface area measurements and H$_2$-temperature programmed reduction (H$_2$-TPR) to evaluate reduction properties and metal–support interactions. High-resolution transmission electron microscopy (HR-TEM) provided insights into the morphology, while X-ray photoelectron spectroscopy (XPS) was used to assess surface chemical

states. Additional analysis included O_2 and CO_2 temperature-programmed desorption (O_2-TPD and CO_2-TPD, respectively) to study adsorption and desorption behaviors. Raman spectroscopy was employed to investigate vibrational modes and structural defects and thermogravimetric analysis (TGA) was used for thermal stability/coke study assessment. Detailed descriptions of these characterization methods and procedures can be found in the ESI.†

Catalytic activity

The activity test for CO_2 reforming of methane was conducted at atmospheric pressure using a fixed bed down flow reactor. A comprehensive description of the procedure is available in the ESI.† The conversions were calculated using eqn (1) and (2) and the syngas ratio was determined using eqn (3)

$$X_{CH_4}(\%) = \frac{(n_{CH_4\,in} - n_{CH_4\,out})}{n_{CH_4\,in}} \times 100 \tag{1}$$

$$X_{CO_2}(\%) = \frac{(n_{CO_2\,in} - n_{CO_2\,out})}{n_{CO_2\,in}} \times 100 \tag{2}$$

$$\frac{H_2}{CO} = \frac{n_{H_2\,out}}{n_{CO\,out}} \tag{3}$$

Results and discussion

Catalyst characterization

Fig. 1 illustrates the XRD patterns of fresh 5NZ, 5NC and 5NCZ catalysts. The XRD pattern of the 5NZ catalyst exhibits characteristics peaks of both monoclinic (ZrO_2-m) and tetragonal (ZrO_2-t) phases of ZrO_2.[43–46] The tetragonal phase is identified by distinct diffraction peaks at 2θ values of approximately 30.5°, 34.7°, 35.6°, 50.5°, 50.9°, 59.6°, 60.4°, 63.1° and 74.7° (JCPDS card no. 88-1007).[41,45,47] Meanwhile, the monoclinic phase is identified by the diffraction peaks at 2θ values of approximately 28.4°, 31.7°, 41.1°, 35.5°, 41.2°, 45.6°, 49.5°, 54.1°, 55.8° and

57.3° (JCPDS card no. 83-0943).[44,46] However, the tetragonal phase is more predominant than the monoclinic phase. The XRD pattern of fresh 5NC and 5NCZ catalysts exhibits the distinct cubic fluoride phase of CeO_2 having the $Fm\bar{3}m$ space group.[48] The major peaks for 5NC were observed at 28.4°, 33.1°, 42.6°, 47.5°, 56.3°, 59.1°, 69.4°, 76.7° and 79.1° (JCPDS card no. 81-0792).[16] It is important to highlight that the diffraction pattern of the 5NCZ catalyst shows a single phase of cubic fluorite CeO_2 with a slight shift towards higher 2θ values. This indicates the creation of a CeO_2–ZrO_2 solid solution. Additionally, the diffraction pattern of the 5NCZ sample does not show any peaks associated with ZrO_2 phases.

The inset of Fig. 1 provides a close-up view of the most intense (111) plane for the 5NC and 5NCZ catalysts. For the 5NCZ catalyst, peaks were detected at 2θ values of 28.82°, 33.4°, 43.0°, 47.9°, 56.8°, 59.5°, 70.1°, and 77.5°, which are notably higher than the corresponding 2θ Bragg angles for the 5NC catalyst. The shift toward higher Bragg angles indicates the inclusion of Zr^{4+} into the CeO_2 lattice. This substitution results in a decrease in interplanar spacing and lattice strain, as the smaller Zr^{4+} ions (0.84 Å) replace the larger Ce^{4+} ions (0.97 Å) within the lattice.[41,49] Lattice distortion, involving contraction or deformation, often results in oxygen vacancies, enhancing the oxygen storage capacity and oxygen mobility.[48,49] The crystallite sizes of 5NZ, 5NC and 5NCZ catalysts were estimated to be 17.1 nm, 15.7 nm and 10.8 nm, respectively. The XRD patterns of the 30-hour spent 5NZ, 5NC, and 5NCZ samples are displayed in Fig. S1 (ESI†). The spent 5NC and 5NCZ catalysts show no significant changes in their XRD patterns. However, metallic Ni (JCPDS card no. 87-0712) is detected in the 5NC and 5NCZ catalysts, while NiO (JCPDS card no. 78-0643) appears in the 5NZ catalyst. Notably, the 5NCZ catalyst exhibits significantly lower diffraction peak intensity compared to 5NC and 5NZ, indicating superior thermal stability.

Table 1 presents the BET surface area and Ni content (determined by ICP-AES) for each synthesized catalyst, offering key insights into their catalytic performance. The results indicate that the elemental composition of all catalysts is in close agreement with the nominal input values. The BET surface area of the fresh catalyst ranges from 44 to 49 m² g⁻¹, with only minor variations. After the reaction, the 5NZ catalyst showed the greatest decrease in surface area, followed by 5NC, while the 5NCZ catalyst exhibited a minimal decrease. This indicates superior stability, likely due to the formation of a CeO_2–ZrO_2 solid solution.
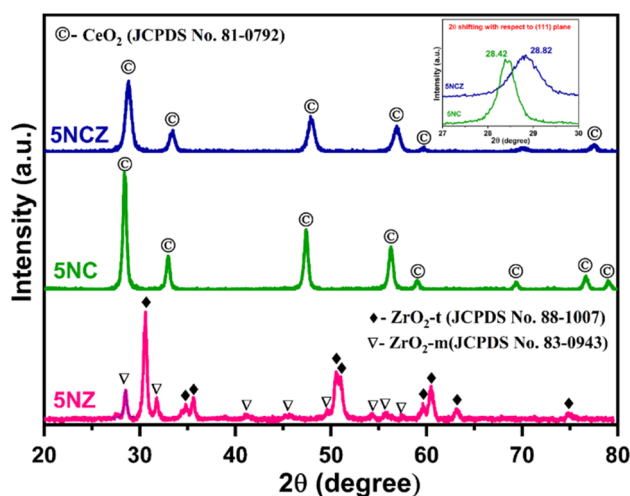

Fig. 1 XRD patterns of 5NZ^{fresh}, 5NC^{fresh} and 5NCZ^{fresh} catalysts.

Table 1 Ni content and surface area of the synthesized samples

Catalyst	Ni loading (%) in fresh samples	BET surface area (m² g⁻¹)	
		Fresh	Spent (30 h)
5NZ	4.97	44	17
5NC	4.94	40	28
5NCZ	4.93	49	41

The TEM/HR-TEM images of the reduced 5NCZ sample are displayed in Fig. 2a–c. The catalyst displayed irregular spherical nanoparticles that are closely interconnected (Fig. 2a). Statistical analysis (inset of Fig. 2a) of the particle sizes indicated that the nanoparticles have an average size of 8.5 nm ranging from 6 to 12 nanometers, suggesting a fairly uniform size distribution. Additionally, the lattice fringes observed in the TEM image provided insights into the crystal structure of both $Ce_{0.8}Zr_{0.2}O_{2-x}$ and Ni nanoparticles. The lattice fringes with d-spacing values of 0.27 and 0.31 nm, as shown in Fig. 2b and c, correspond to the (200) and (111) planes of cerium oxide, respectively, within the crystal lattice. Additionally, the d spacing value of 0.20 nm, visible in Fig. 2c, is associated with the interplanar spacing of the (111) planes of Ni^0 species.

The selective area electron diffraction (SAED) pattern further validated the crystalline nature and cubic fluorite phase of CeO_2 oxide, as illustrated in Fig. 2d. Elemental mapping of the 5NCZ catalyst exhibited the homogenous and uniform distribution of Ce, Zr, Ni and O elements, as shown in Fig. S2.† The TEM images and SAED pattern of spent (30 h) 5NCZ are depicted in Fig. 2a–c, respectively, showing no significant changes in morphology and coke deposition. The cubic fluorite phase is also consistent in the spent catalyst, as illustrated by the SAED pattern.

The H_2-TPR profiles of the 5NZ, 5NC and 5NCZ catalysts were acquired to obtain insights into the reducibility and the metal–support interactions. These patterns are illustrated in Fig. 3. The TPR graphs of all the samples displayed a broad peak (α), which may be ascribed to the H_2 consumption by active oxygen species (O_2^{2-} and O_2^-) adsorbed at oxygen vacancy sites. Active oxygen species are formed as a result of incorporating low-valent/small cations into the ceria lattice, and these species
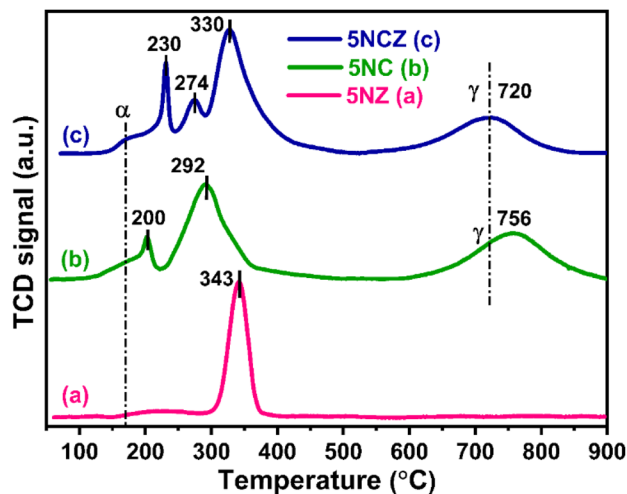

Fig. 3 TPR graphs of 5NZ (a), 5NC (b) and 5NCZ (c) samples.

can be reduced at low temperatures.[16,50,51] For the 5NZ catalyst, a single peak observed at 343 °C corresponds to the reduction of strongly interacting NiO with the ZrO_2 support.[52] ZrO_2 is a non-reducible support; hence no further peaks were observed for the 5NZ catalyst.[52,53] The reduction patterns of the 5NC and 5NCZ catalysts show multiple peaks corresponding to the reduction of NiO species with varying degrees of interaction. The 5NC catalyst exhibits two peaks at 200 and 292 °C, which are attributed to the reduction of well-dispersed and strongly interacting NiO species, respectively. In contrast, the 5NCZ catalyst displays three peaks at 230, 274 and 330 °C. The first two peaks correspond to the reduction of well-dispersed NiO species, while the high-temperature peak is associated with NiO species exhibiting strong metal–support interactions.[54] The elevated temperature observed for the 5NCZ catalyst, compared to the pure ceria sample (5NC), suggests a strong metal–support interaction, likely due to the incorporation of zirconia.

According to J. Lin et al., the high-temperature peak typically reflects strong interactions between Ni and the support.[40,55] In such samples, NiO initially occupies the most active surface sites of the support, forming a thermodynamically stable state, and its uniform dispersion on the support makes it more resistant to reduction, resulting in higher reduction temperatures.[40,56] Based on the reduction temperatures and patterns of NiO species shown in Fig. 3, the 5NCZ catalyst exhibits a greater degree of strong metal–support interaction compared to the others. Furthermore, 5NC and 5NCZ catalysts also show a higher temperature reduction peak, denoted as γ, which is attributed to the reduction of bulk oxygen of CeO_2 and $Ce_{0.8}Zr_{0.2}O_{2-x}$ supports, respectively. The lower reduction temperature (720 °C) for bulk oxygen in the 5NCZ catalyst compared to the 5NC (756 °C) catalyst, indicates easier bulk oxygen reduction. This ease of reduction could be due to the incorporation of Zr^{4+} into the ceria lattice, which enhances oxygen mobility and reduces the energy required to remove lattice oxygen. The total H_2 consumption for all the catalysts is categorized into two regions, 100–500 °C and 500–900 °C, attributed to the H_2
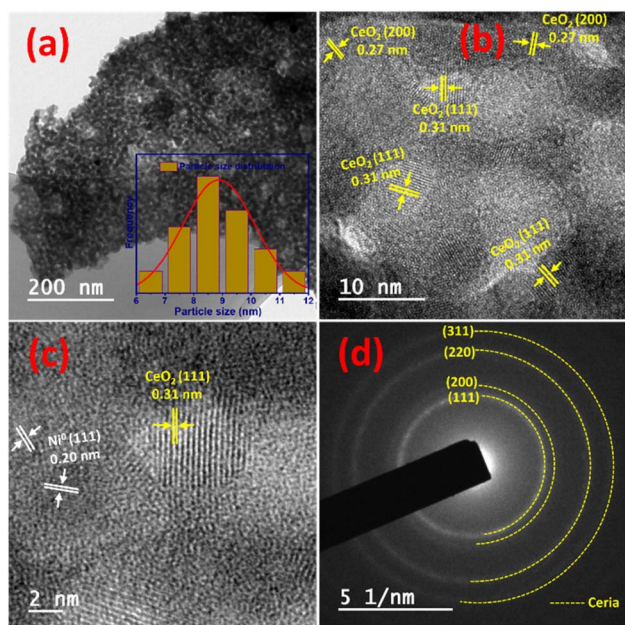

Fig. 2 TEM image (a), HR-TEM images (b and c) and the SAED pattern (d) of the freshly reduced 5NCZ catalyst.

consumption by the NiO species along with active oxygen species and lattice oxygen, respectively (Table S1†).

Raman spectra provide a general overview of the detailed structural insights into defects and lattice distortions of the freshly synthesized catalysts, as shown in Fig. 4. The Raman spectra of pure Ni/ZrO$_2$ (5NZ) reveal both tetragonal and monoclinic phases, corroborated by XRD results. The Raman-active bands at 75 (A$_{1g}$), 149 (E$_g$), 272 (A$_{1g}$), 320 (B$_{1g}$), 470 (E$_g$), 602 (B$_{1g}$) and 647 cm^{-1} (E$_g$) are attributed to the tetragonal phase.[41,45,57] Meanwhile, the bands at 107 (A$_g$), 179 (A$_g$ + B$_g$), 193 (A$_g$), 226 (B$_g$), 344 (A$_g$), 385 (B$_g$), 479 (A$_g$), 506 (B$_g$), 540 (B$_g$), 563 (A$_g$) and 620 cm^{-1} (B$_g$) are attributed to the monoclinic phase of ZrO$_2$.[57,58] In 5NC and 5NCZ catalysts, the most intense bands at 459.7 and 470.3 cm^{-1} are characteristic of the triply degenerate F$_{2g}$ mode, corresponding to the symmetrical stretching of the Ce–O bonds in the fluorite structure of CeO$_2$.[16,50,59] The presence of oxygen vacancies often leads to peak broadening and shifts in the F$_{2g}$ mode. Additional peaks or shoulders may appear due to local distortions and changes in the lattice symmetry caused by these vacancies.[16,32,60] The peak broadening and gradual shift in the F$_{2g}$ band in the 5NCZ catalyst from 459.7 to 470.3 cm^{-1} reflect a cell contraction, which results from the incorporation of zirconia into the ceria lattice.[61,62] Substitution of Ce^{4+} with Zr^{4+} shortened the Ce–O bond length, leading to a higher energy shift in the Raman spectra.[41] The broad band in the 530–710 cm^{-1} range is observed in both 5NC and 5NCZ catalysts, with greater intensity in 5NCZ. This defect-induced band (D) arises from the symmetrical vibrations associated with oxygen vacancies.[2,41,63] A weak 2TA band at 235 cm^{-1}, indicative of defect-induced second-order scattering involving TA (transversal acoustic) phonon modes, is observed. This band, typically absent in pure ceria, supports the notion that the ceria lattice becomes defective due to solid solution formation.[16,64] The integrated areas of the D and F$_{2g}$ bands (I_D/$I_{F_{2g}}$ ratio) reflect the

strength of oxygen vacancies in 5NC and 5NCZ catalysts, with the ratio being higher for 5NCZ (0.29) compared to 5NC (0.18). The broad peak at ~1170 cm^{-1} corresponds to vibrational modes specific to superoxide species.[50,65]

The chemical states of ceria-based catalysts and surface oxygen vacancies significantly influence the oxidation/reforming reactions. Fig. 5 shows the Ce 3d XPS spectra of 5NC and 5NCZ catalysts. The Ce 3d XPS spectra consist of two multiplets, labeled u and v, corresponding to the spin–orbit splitting of the 3d$_{5/2}$ and 3d$_{3/2}$ components.[16,41] In the Ce 3d spectrum of ceria, contributions from Ce^{4+} and Ce^{3+} states can be distinguished, each showing distinct peaks. The Ce 3d spectra can be deconvoluted into ten peaks. Specifically, the two spin–orbit doublet peaks, identified as u, u'', v, and v'' correspond to the Ce^{3+} species (red color). Meanwhile, the remaining six peaks labeled u', u''', u'''', v', v''' and v'''' are associated with the Ce^{4+} species.[2,41,50,61] The relative surface concentration of Ce^{3+} is estimated by XPS analysis using the following equation.

$$Ce^{3+}(\%) = \frac{[A(Ce^{3+})]}{[A(Ce^{3+}) + A(Ce^{4+})]} \times 100$$

In this context, $A(Ce^{3+})$ and $A(Ce^{4+})$ denote the overall cumulative areas of the peaks associated with Ce^{3+} and Ce^{4+}, respectively. The proportion of Ce^{3+} for the NC^{fresh} catalyst was estimated to be 29.4%, which significantly increased to 58.8% in the NCZ^{fresh} catalyst after Zr doping. These findings suggest that incorporating Zr promotes the generation of Ce^{3+} on the surface of the CeO$_2$ catalyst,[66] which is associated to the formation of CeO$_2$–ZrO$_2$ solid solution.[61] The substitution of Ce^{4+} ions (0.97 Å) in CeO$_2$ with larger Ce^{3+} ions (1.10 Å) can offset the lattice contraction caused by the slightly smaller Zr^{4+} ions (0.84 Å).[41,67] Interestingly, the Ce 3d core level XPS spectra of the spent 5NCZ catalyst exhibit no notable alterations in the fundamental spectra or Ce^{3+} concentration, demonstrating the exceptional stability of the 5NCZ catalyst.
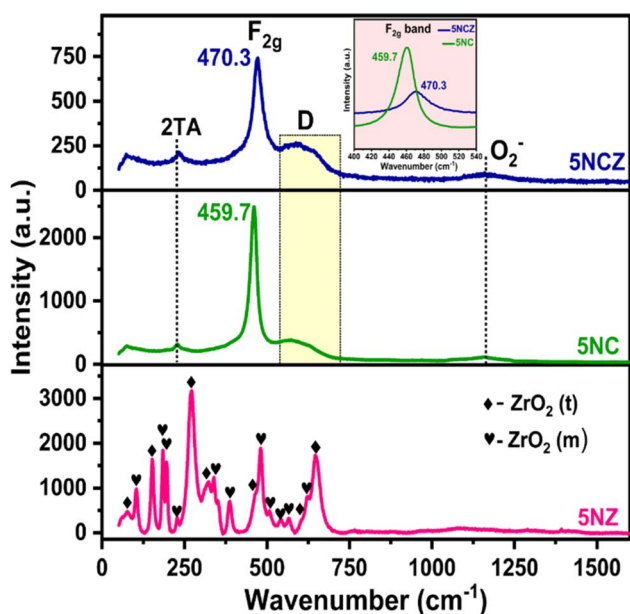

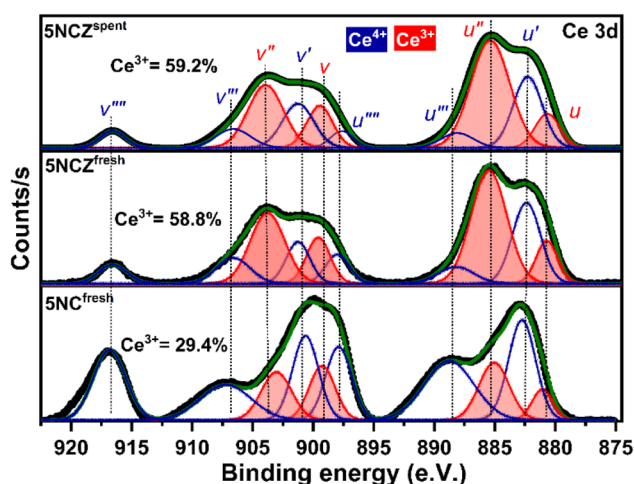Fig. 4 Raman spectra of 5NZ^{fresh}, 5NC^{fresh} and 5NCZ^{fresh} catalysts.

Fig. 5 Ce 3d core level XPS spectra of 5NC^{fresh}, 5NCZ^{fresh} and 5NCZ^{spent} catalysts.
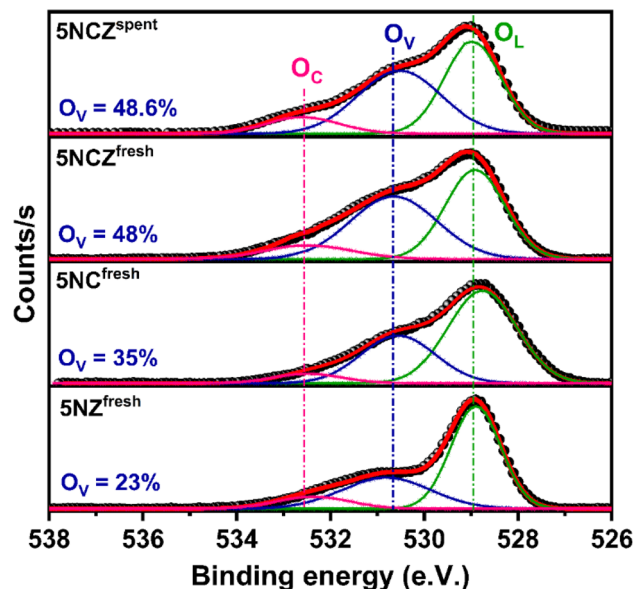
Fig. 6 O 1s XPS spectra of 5NZ^{fresh}, 5NC^{fresh}, 5NCZ^{fresh} and 5NCZ^{spent} catalysts.

The chemical states (Ce^{3+} ratio) of ceria-based catalysts significantly influence the surface oxygen vacancies. Therefore, O 1s core level XPS was conducted for all the synthesized catalysts to gain further insights into the surface oxygen properties, as displayed in Fig. 6. The O 1s spectra can be deconvoluted into three distinct peaks, designated as O$_L$ at 529.0 eV, O$_V$ at 530.7 eV and O$_C$ at 532.6 eV, which correspond to lattice oxygen, oxygen vacancies and chemisorbed oxygen species, respectively.[41,68] The amount of surface oxygen vacancies in the catalysts can be estimated by analyzing the integrated peak areas of all the distinct peaks using the following equation.

$$O_V(\%) = \frac{[A(O_V)]}{[A(O_L) + A(O_V) + A(O_C)]} \times 100$$

where $A(O_L)$ is the integrated area of O$_L$, $A(O_V)$ is the integrated area of O$_V$ and $A(O_C)$ is the integrated area of O$_C$. A 13% increase in oxygen vacancies was observed in the 5NCZ catalyst after incorporating Zr. The proportion of oxygen vacancies (O$_V$%) was estimated to be the highest for fresh 5NCZ (48.0%), followed by 5NC (35%) and 5NZ (23%) catalysts. The 12% increase in oxygen vacancies from the 5NZ catalyst to the 5NC catalyst, despite the same Ni loading, is likely due to the redox behavior of ceria; the addition of Ni into the ceria lattice may enhance the transition from Ce^{3+} to Ce^{4+}. The proportion of oxygen vacancies in the spent 5NCZ catalyst remained largely unchanged, as illustrated in Fig. 6.

The Ni 2p core level and Zr 3d core level XPS spectra of the 5NCZ catalyst are shown in Fig. 7a and b, respectively. Two type of Ni species, Ni^0 and Ni^{2+} species at the binding energy values at 852.8 and 855.7 eV, respectively, was observed in both the fresh and spent 5NCZ catalyst, as demonstrated in Fig. 7a.[40,42] The slightly higher binding energy for Ni^{2+} (855.7 eV) compared to bulk NiO (854.2 eV) can be attributed to strong metal–support interactions. This increase in binding energy likely results from the incorporation of Ni^{2+} species into the host lattice.[69] The peak that appeared at 861.3 eV is due to the satellite peak.

The core level XPS spectra of Zr 3d in Fig. 7b display two peaks at binding energies of 182.0 and 184.4 eV, corresponding to Zr^{4+} species present in both the fresh and spent 5NCZ catalysts.[41,44] The energy separation between the Zr 3d$_{5/2}$ and Zr 3d$_{3/2}$ peaks is consistent with the value observed for Zr^{4+} (Δ = 2.4 eV).[45] The binding energies values (182.0 and 184.4 eV) for Zr^{4+} species in the 5NCZ catalyst are slightly higher than those observed in pure ZrO$_2$ (Fig. S4†), further confirming the hypothesis that Zr species have been incorporated into the ceria lattice, forming a CeO$_2$–ZrO$_2$ solid solution.[67,70] The Zr 3d and Ni 2p core level XPS spectra of the spent 5NCZ catalyst closely resemble those of the fresh catalyst, with a minor increase in Ni^0 content in the spent sample.

The surface basicity of catalysts plays a pivotal role in determining their efficiency in reactions such as CO$_2$ hydrogenation and dry reforming of methane.[2,71,72] To investigate the
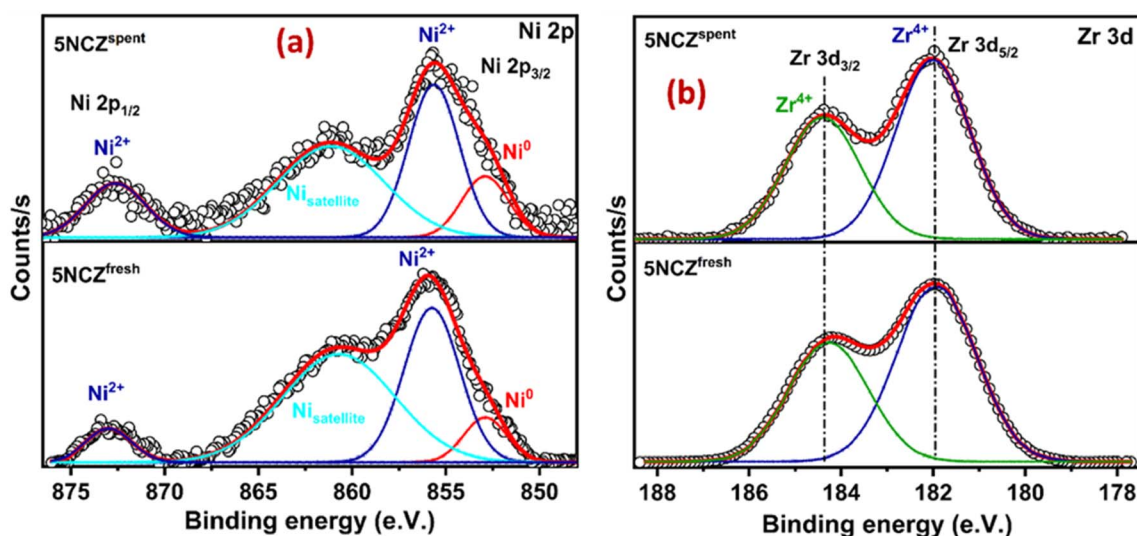

Fig. 7 Ni 2p (a) and Zr 3d (b) XPS spectra of fresh and spent 5NCZ catalysts.
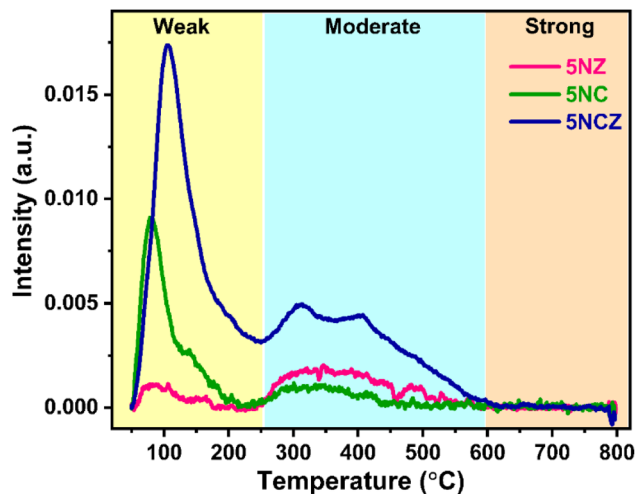
Fig. 8 CO_2-TPD patterns of the synthesized 5NZ, 5NC and 5NCZ catalysts.

Fig. 9 O_2-TPD patterns of the synthesized 5NZ (a), 5NC (b) and 5NCZ (c) catalysts.

basic strength of the synthesized catalyst, CO_2-TPD was performed, as shown in Fig. 8. The CO_2-TPD profiles of the samples typically show multiple desorption peaks, reflecting the diversity of basic sites. The TPD profile, indicating the varying strengths of CO_2 interaction with the catalyst surface, can be divided into three zones: weak basic sites (<250 °C), moderate basic sites (250–550 °C) and strong basic sites (>550 °C).[50,73] All catalysts exhibited significant CO_2 desorption in the weak and moderate regions, indicating the existence of weak and moderate basic sites on the catalyst surface. It should be noted that while all types of basic sites facilitate CO_2 adsorption, weak and moderate sites are essential for CO_2 adsorption, desorption and product formation. In contrast, strong basic sites, which are prone to coke formation, are less suitable for stable DRM reactions.[5,16] The quantification of basic sites across these regions is detailed in Table 2. The 5NCZ catalyst possesses the highest number of total basic sites (75.5 µmol g^{-1}), followed by the 5NC (23.7 µmol g^{-1}) and 5NZ (12.9 µmol g^{-1}) catalysts. The substantial increase in basic sites in the 5NCZ catalyst is attributed to the higher number of defects and oxygen vacancies. The quantity of basic sites aligns with the trend of these defect sites and vacancies.

The catalyst's capacity to absorb oxygen is a critical factor in demonstrating enhanced activity. The O_2-TPD desorption profile can differentiate the various oxygen species on the ceria surface, including surface oxygen, oxygen vacancies and lattice
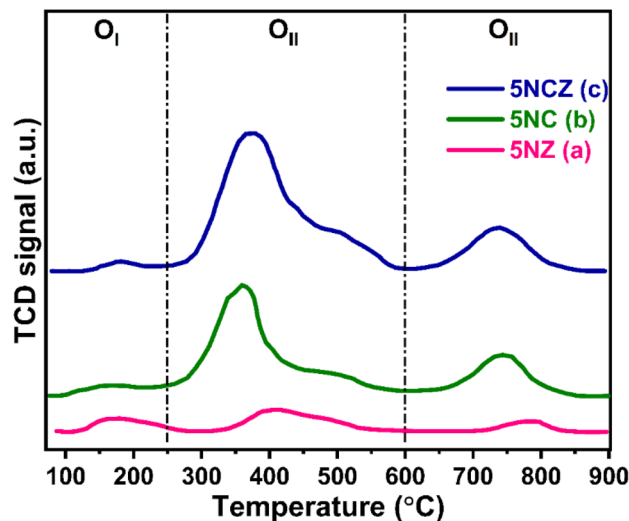
oxygen.[50,74] In this context, the O_2-TPD was performed for the 5NZ, 5NC and 5NCZ catalysts and the results are depicted in Fig. 9. The O_2-TPD pattern reveals three distinct desorption regions: 100–250 °C for superficial or weakly bound oxygen, 250–600 °C for active oxygen species (O_2^{2-} and O_2^-) at vacancy sites and above 600 °C for lattice oxygen (O^{2-}).[2,10,75] The quantification of oxygen species in each region, based on the integrated peak areas, is detailed in Table 3. The quantity of O_2 desorbed in the O_{II} region is directly proportional to the concentration of active oxygen species in that sample and follows the order: 5NCZ > 5NC > 5NZ.

Active oxygen species (O_2^{2-} and O_2^-) serve as active centers for CH_4 and CO_2 activation to produce syngas selectively while inhibiting coke deposition.[16,25] The trend in active oxygen species approximated by O_2-TPD is consistent with the results from O 1s core level XPS and Raman analysis, reinforcing this conclusion. The amount of O_{II} species estimated by O_2-TPD was plotted against catalytic activity, to establish a correlation, where a linear relation was obtained (discussed later).

Catalytic performance

The catalytic performance and stability tests for CO_2 reforming of methane were conducted to assess and compare the performance of all synthesized catalysts. Table S2† compares the synthesized catalysts with other reported Ni-based catalysts in

Table 2 Basic site distribution estimated by CO_2-TPD

	Quantity of basic sites (µmol g^{-1})		
Catalyst	Weak region	Moderate region	Total amount of basic sites
5NZ	2.2	10.7	12.9
5NC	15.6	8.1	23.7
5NCZ	54.1	21.4	75.5

Table 3 Types of oxygen species estimated from O_2-TPD analysis

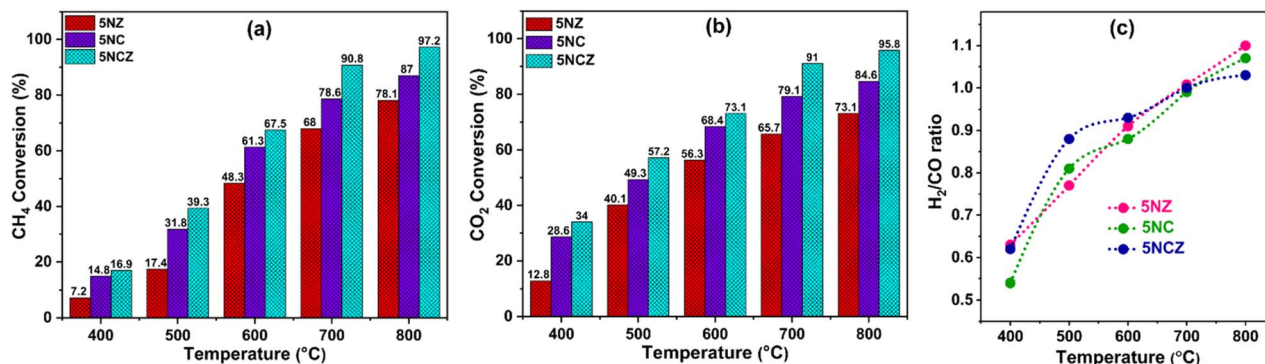|	Quantity of desorbed oxygen in µmol g^{-1}			
Catalyst	O_I	O_{II}	O_{III}	Total
5NZ	3.9	7.6	2.7	14.2
5NC	3.1	26.2	10.3	39.6
5NCZ	2.5	47.3	12.1	61.9

Fig. 10 Temperature effect on methane and carbon dioxide conversion (a and b) and the H_2/CO ratio (c) over the 5NZ, 5NC and 5NCZ samples (activity test conditions: feed ratio-$CH_4 : CO_2 : N_2 - 1 : 1 : 8$, GHSV-50 000 mL h^{-1} g^{-1}, pressure-1 atm, and time-5 h).

terms of conversion, H_2/CO ratio and stability. The impact of temperature was studied within the range of 400–800 °C. The results, focusing on feed conversion and the H_2/CO ratio in syngas, are presented in Fig. 10a–c, respectively. Since, DRM is an endothermic reaction, higher feed conversions can only be achieved at elevated temperatures.[4] As the temperature rises, the conversion rates of CO_2 and CH_4 progressively increase. The 5NZ catalyst demonstrated the lowest conversion rate, whereas the 5NC catalyst exhibited a marginally higher conversion rate across all temperatures. However, the 5NCZ catalyst achieved the highest conversion rate and an improved H_2/CO ratio compared to both the 5NC and 5NZ catalysts, indicating that a significant synergistic effect occurred after incorporating ZrO_2 into the ceria lattice. The anticipated value of the H_2/CO ratio in the DRM reaction is one; however, at low temperatures, the H_2/CO ratio is <1, as illustrated in Fig. 10c. A low H_2/CO ratio (<1) suggests the occurrence of the reverse water gas shift reaction (RWGS), which is further evidenced by the higher CO_2 conversion compared to CH_4 at lower temperatures.[4,31] As the temperature increases, the syngas ratio improves, with DRM becoming the dominant reaction at 700 °C, resulting in an H_2/CO ratio close to unity. However, at higher temperatures, methane decomposition becomes more favorable, leading to a syngas H_2/CO ratio greater than one.[2,16] The H_2 and CO selectivity of the synthesized catalysts at 700 °C is shown in Fig. S6.†

Fig. 11 illustrates the effect of nickel loading (wt%) on feed conversion and H_2/CO in the $Ni/Ce_{0.8}Zr_{0.2}O_{2-x}$ (NCZ) catalyst. The NCZ catalyst was prepared by varying the Ni wt% from 2.5–7.5% for comparison purposes. The H_2 and CO selectivity of 2.5NCZ, 5NCZ and 7.5NCZ at 700 °C is provided in Fig. S7.† The feed conversion and H_2/CO ratio increase when Ni loading increases from 2.5 to 5 wt%, but beyond this point, there is no significant increase in feed conversion. However, the H_2/CO ratio increases, resulting from high methane conversion compared to CO_2. Hence, 5 wt% Ni is considered as optimum loading.

It is essential to highlight that oxygen vacancies (O_V)/active oxygen species (O_{II}) are pivotal in influencing both the catalytic activity and the syngas selectivity in DRM.[16] The catalytic activity, in terms of conversion rates, showed a linear
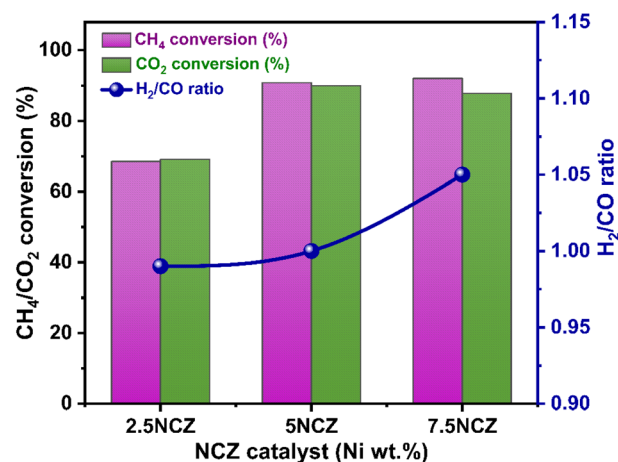

Fig. 11 Effect of Ni loading in terms of conversions and the H_2/CO ratio over the NCZ catalyst.

relationship with the concentrations of O_V and O_{II} species, which were determined from O 1s XPS and O_2-TPD analysis, respectively. This investigation was conducted to elucidate the structure–activity relationship, as depicted in Fig. 12a and b. The 5NCZ catalyst, which contains a higher amount of O_V and O_{II} species, exhibited the highest conversions.

The time-on-stream (TOS) test was conducted to check the stability of the synthesized catalyst. Fig. S5(a and b)† show the 30 h TOS test over the 5NZ, 5NC and 5NCZ catalysts. The 5NCZ catalyst showed stable performance throughout the reaction, while 5NZ and 5NC catalysts showed a significant decrease in their activity. The 5NC catalyst exhibited lower deactivation compared to 5NZ. The 5NZ catalyst showed decreases of ~15.8% and 18% in methane and CO_2 conversion while the 5NC catalyst showed decreases of 10.2% and 11.4% in methane and CO_2 conversion, respectively. The cause of deactivation was determined through coke analysis. The TGA pattern of the spent samples (30 h) are provided in Fig. 13a. The analysis reveals weight losses of 1.2%, 7.0%, and 13.8% for the 5NCZ, 5NC, and 5NZ catalysts, respectively. The 5NCZ catalyst experiences a modest 1.2% weight loss up to ~350 °C, likely due to the removal of physically adsorbed water or moisture,[15] with no
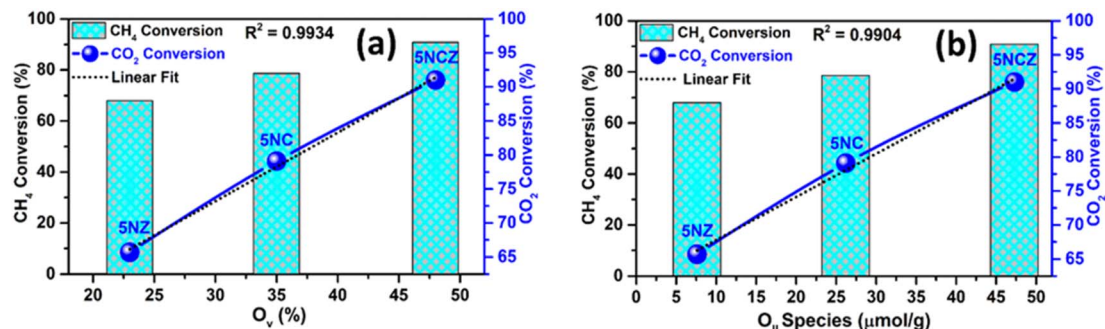
Fig. 12 Structure−activity correlation: oxygen vacancy (O_V) ratio *vs.* CH_4 and CO_2 conversion (a) and oxygen species (O_{II}) ratio *vs.* CH_4 and CO_2 conversion (b).
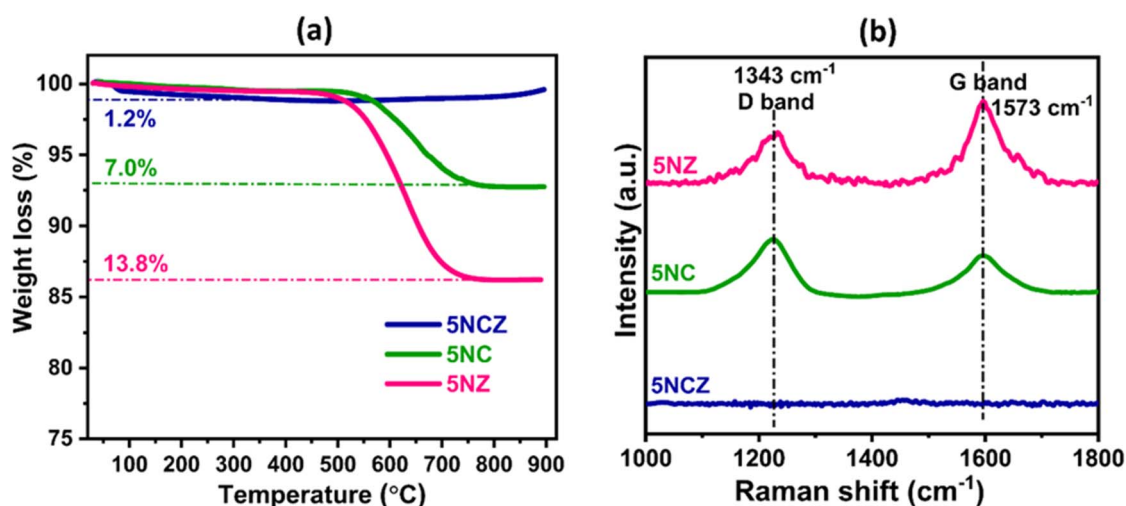

Fig. 13 TGA patterns (a) and Raman spectra of spent 5NZ, 5NC and 5NCZ catalysts (b).

further weight loss observed beyond this point. Interestingly, a slight weight gain is observed above 400 °C, which could be attributed to the oxidation of Ni^0 and ceria in the presence of oxygen environment. For the 5NC and 5NZ catalysts, weight loss continues up to 750 °C, which is indicative of coke removal.[54] To further explore the nature of the deposited coke, Raman analysis was conducted and the results are shown in Fig. 13b. The 5NCZ catalyst exhibited no significant bands, reinforcing that the 1.2% weight loss is likely due to the desorption of water. Conversely, the 5NC and 5NZ catalysts exhibit both D and G bands at approximately 1343 and 1573 cm^{-1}, respectively. The D band corresponds to disordered or amorphous coke, while the G band is related to ordered or graphitic coke.[40,76] The I_D/I_G ratio, which indicates the extent of graphitization,[40] is estimated to be 1.38 for the 5NC catalyst and 0.62 for the 5NZ catalyst. The lower I_D/I_G ratio for the 5NZ catalyst suggests a higher degree of graphitization.[40] The 5NC catalyst, with a high I_D/I_G ratio, demonstrates that the ceria support effectively reduces the formation of graphitic coke.

The 5NCZ catalyst exhibited remarkable activity, approximately 90.8% and 91.0% conversion of methane and CO_2, respectively, with an H_2/CO ratio of unity at 700 °C. Therefore, a 100 h TOS stability test was performed over the 5NCZ catalyst,

as shown in Fig. 14. The catalyst demonstrated consistent activity up to 100 h without any significant deactivation, showing the excellent stability of the 5NCZ catalyst. The
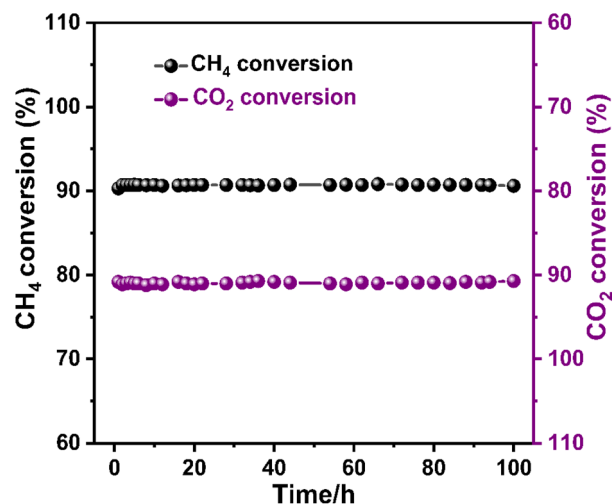

Fig. 14 100 h stability test over the 5NCZ catalyst (reaction condition: temperature-700 °C, pressure-1 atm, GHSV-50 000 mL g^{-1} h^{-1}, and feed ratio $CH_4 : CO_2 : N_2$-1 : 1 : 8).

schematic presentation of the reaction set-up for dry reforming of methane is shown in Fig. S8.†

In the 5NCZ catalyst, Ni sites are responsible for activating CH_4 by breaking C–H bonds, while the CeO_2–ZrO_2 support offers oxygen storage and release capacity, promotes CO_2 activation and resists coke formation. For the plausible mechanism of DRM over the 5NCZ (5% Ni/$Ce_{0.8}Zr_{0.2}O_{2-x}$) catalyst, CH_4 activation and CO_2 activation are the two crucial steps which lead to the product formation. Methane molecules can adsorb onto the Ni sites, where dissociative adsorption occurs *via* C–H bond elongation from the reactant state to the transition state, leading to the formation of CH_x ($x = 1$–3) species and hydrogen. The metallic Ni sites facilitate the cleavage of the C–H bond due to their excellent catalytic properties for hydrocarbon activation.[2,77,78]

Similar to CH_4 activation, the activation of CO_2 is also important for catalyst activity in the DRM reaction. CO_2 adsorption and activation occur predominantly at the $Ce_{0.8}Zr_{0.2}O_{2-x}$ support, particularly at oxygen vacancy sites. Our recent study revealed that CO_2 is adsorbed and activated at the oxygen vacancies, leading to the formation of CO and O* species (active oxygen species).[16] This step is crucial for generating active oxygen species (O*) that assist in methane reforming and carbon removal. These O* species generated on the $Ce_{0.8}Zr_{0.2}O_{2-x}$ surface readily react with CH_x species or carbon deposits on the Ni surface, preventing catalyst deactivation and promoting the formation of CO.[77] Concurrently, hydrogen atoms produced during methane dissociation recombine at Ni sites to form H_2 molecules. The reaction proceeds through the continuous interaction of dissociated CH_x species with oxygen intermediates, yielding CO and H_2 as the primary products. The stability of the $Ce_{0.8}Zr_{0.2}O_{2-x}$ support ensures sustained generation and utilization of oxygen vacancies throughout the reaction.

Conclusion

This research focuses on exploring the performance of 5% Ni/ZrO_2 (5NZ), 5% Ni/CeO_2 (5NC), and 5% Ni/$Ce_{0.8}Zr_{0.2}O_{2-x}$ (5NCZ) catalysts synthesized by a straightforward one-pot complex combustion method for CO_2 reforming of methane (DRM). The 5NZ catalyst demonstrated moderate activity for DRM, but suffered from significant deactivation over time, attributed to rapid sintering of nickel particles and carbon deposition. The 5NC catalyst showed improved stability and higher activity compared to the 5NZ catalyst. The presence of ceria enhanced the redox properties of the catalyst, promoting better oxygen mobility and preventing excessive carbon deposition, especially graphitic carbon, as shown by Raman analysis. The high I_D/I_G ratio in the 5NC catalyst compared to 5NZ catalyst indicated lower degree of graphitization. The 5NCZ catalyst, combining both ceria and zirconia, exhibited the best overall performance among the three. The 5NCZ showed 90.8% and 91.0% methane and CO_2 conversion, respectively, with a H_2/CO ratio of one at 700 °C. These dual-functional catalysts benefited from the synergistic effects of ceria and zirconia, leading to better thermal stability and redox properties. The performance

improvement in the 5NCZ sample is attributed to the formation of a CeO_2–ZrO_2 solid solution. The formation of the solid solution was validated by the XRD and Raman analysis, as no peaks/bands attributed to ZrO_2 species were observed. The progressive shift in the 2θ Bragg angle compared to the pure CeO_2 sample (28.42–28.82°) confirmed the lattice contraction and decrease in crystallite size. A shift towards higher binding energy for Zr 3d core level XPS spectra compared to the pure ZrO_2 sample, further confirms the inclusion of Zr species into the ceria lattice. The formation of the CeO_2–ZrO_2 solid solution remarkably enhanced oxygen vacancies and O_{II} species. Incorporating zirconia also enhanced the metal–support interaction and increased both the quantity and strength of basic sites. The resulting catalyst not only showed superior activity but also maintained stability and selectivity for an extended period (100 h), making it the most effective choice for DRM among the tested catalysts.

Data availability

All data supporting the findings of this study are available within the article and its ESI.† Additional data related to this study will be made available on suitable request.

Author contributions

Rubina Khatun – designed and performed the experiments for the research work, manuscript writing, editing and correction; Rohan Singh Pal – reaction analysis and catalyst characterization; Kapil Bhati, Anil Chandra Kothari, Shivani Singh, Nazia Siddiqui, and Swati Rana contributed in catalyst characterization; Rajaram Bal – conceptualization and design of the whole study, design of experiments for the research work, manuscript correction.

Conflicts of interest

The authors declare no conflicts of interest.

Acknowledgements

References

1 M. Li and A. C. van Veen, *Appl. Catal., B*, 2018, **237**, 641–648.
2 R. Khatun, N. Siddiqui, R. S. Pal, S. Bhandari, T. S. Khan, S. Singh, M. K. Poddar, C. Samanta and R. Bal, *Catal. Sci. Technol.*, 2023, **13**, 6431–6445.
3 B. Erdogan, H. Arbag and N. Yasyerli, *Int. J. Hydrogen Energy*, 2018, **43**, 1396–1405.
4 M. Shah, S. Das, A. K. Nayak, P. Mondal and A. Bordoloi, *Appl. Catal., A*, 2018, **556**, 137–154.

5 R. Zhou, M. Mohamedali, Y. Ren, Q. Lu and N. Mahinpey, *Appl. Catal., B*, 2022, **316**, 121696.

6 T. G. de Araújo Moreira, J. F. S. de Carvalho Filho, Y. Carvalho, J. M. A. R. de Almeida, P. N. Romano and E. F. Sousa-Aguiar, *Fuel*, 2021, **287**, 119536.

7 Z. Liu, D. C. Grinter, P. G. Lustemberg, T. D. Nguyen-Phan, Y. Zhou, S. Luo, I. Waluyo, E. J. Crumlin, D. J. Stacchiola and J. Zhou, *Angew. Chem., Int. Ed.*, 2016, **55**, 7455–7459.

8 Y. Song, E. Ozdemir, S. Ramesh, A. Adishev, S. Subramanian, A. Harale, M. Albuali, B. A. Fadhel, A. Jamal and D. Moon, *Science*, 2020, **367**, 777–781.

9 M. Akri, S. Zhao, X. Li, K. Zang, A. F. Lee, M. A. Isaacs, W. Xi, Y. Gangarajula, J. Luo and Y. Ren, *Nat. Commun.*, 2019, **10**, 5181.

10 Y. Zhang, Y. Zu, D. He, J. Liang, L. Zhu, Y. Mei and Y. Luo, *Appl. Catal., B*, 2022, **315**, 121539.

11 M. A. A. Aziz, H. D. Setiabudi, L. P. Teh, M. Asmadi, J. Matmin and S. Wongsakulphasatch, *Chem. Eng. Technol.*, 2020, **43**, 661–671.

12 M. Shah, P. Mondal, A. K. Nayak and A. Bordoloi, *J. CO2 Util.*, 2020, **39**, 101160.

13 M. Yusuf, A. S. Farooqi, L. K. Keong, K. Hellgardt and B. Abdullah, *Chem. Eng. Sci.*, 2021, **229**, 116072.

14 F. Cheng, X. Duan and K. Xie, *Angew. Chem.*, 2021, **133**, 18940–18947.

15 R. K. Singha, A. Yadav, A. Agrawal, A. Shukla, S. Adak, T. Sasaki and R. Bal, *Appl. Catal., B*, 2016, **191**, 165–178.

16 R. Khatun, R. S. Pal, M. A. Shoeb, D. Khurana, S. Singhl, N. Siddiqui, M. K. Poddar, T. S. Khan and R. Bal, *Appl. Catal., B*, 2024, **340**, 123243.

17 J. Carrasco, D. López-Durán, Z. Liu, T. Duchoň, J. Evans, S. D. Senanayake, E. J. Crumlin, V. Matolín, J. A. Rodríguez and M. V. Ganduglia-Pirovano, *Angew. Chem., Int. Ed.*, 2015, **54**, 3917–3921.

18 H.-S. Roh, H. Potdar, K.-W. Jun, J.-W. Kim and Y.-S. Oh, *Appl. Catal., A*, 2004, **276**, 231–239.

19 N. Laosiripojana and S. Assabumrungrat, *Appl. Catal., A*, 2005, **290**, 200–211.

20 W. Xu, Z. Liu, A. C. Johnston-Peck, S. D. Senanayake, G. Zhou, D. Stacchiola, E. A. Stach and J. A. Rodriguez, *ACS Catal.*, 2013, **3**, 975–984.

21 S. Ali, M. M. Khader, M. J. Almarri and A. G. Abdelmoneim, *Catal. Today*, 2020, **343**, 26–37.

22 J. Wen, Y. Xie, Y. Ma, H. Sun, H. Wang, M. Liu, Q. Zhang and J. Chen, *Fuel*, 2022, **308**, 122008.

23 M. V. Grabchenko, N. V. Dorofeeva, V. A. Svetlichnyi, Y. V. Larichev, V. La Parola, L. F. Liotta, S. A. Kulinich and O. V. Vodyankina, *Nanomaterials*, 2023, **13**, 2641.

24 Y. Bai, K. Sun, J. Wu, M. Zhang, S. Zhao, Y. D. Kim, Y. Liu, J. Gao, Z. Liu and Z. Peng, *Mol. Catal.*, 2022, **530**, 112577.

25 D. Shen, Z. Li, J. Shan, G. Yu, X. Wang, Y. Zhang, C. Liu, S. Lyu, J. Li and L. Li, *Appl. Catal., B*, 2022, **318**, 121809.

26 R. Babakouhi, S. M. Alavi, M. Rezaei, F. Jokar, M. Varbar and E. Akbari, *Int. J. Hydrogen Energy*, 2024, **60**, 503–514.

27 Z. Xu and E. D. Park, *Catalysts*, 2024, **14**, 176.

28 Y. H. Ahmad, A. T. Mohamed, H. A. El-Sayed, A. Kumar and S. Y. Al-Qaradawi, *Int. J. Hydrogen Energy*, 2022, **47**, 41294–41309.

29 T. M. Onn, S. Zhang, L. Arroyo-Ramirez, Y.-C. Chung, G. W. Graham, X. Pan and R. J. Gorte, *ACS Catal.*, 2015, **5**, 5696–5701.

30 P. Scheiber, M. Fidler, O. Dulub, M. Schmid, U. Diebold, W. Hou, U. Aschauer and A. Selloni, *Phys. Rev. Lett.*, 2012, **109**, 136103.

31 M. Shah, M. K. Al Mesfer and M. Danish, *Int. J. Hydrogen Energy*, 2022, **47**, 8867–8874.

32 B. Safavinia, Y. Wang, C. Jiang, C. Roman, P. Darapaneni, J. Larriviere, D. A. Cullen, K. M. Dooley and J. A. Dorman, *ACS Catal.*, 2020, **10**, 4070–4079.

33 I. Luisetto, S. Tuti, C. Romano, M. Boaro, E. Di Bartolomeo, J. K. Kesavan, S. S. Kumar and K. Selvakumar, *J. CO2 Util.*, 2019, **30**, 63–78.

34 D. Guo, Y. Lu, Y. Ruan, Y. Zhao, Y. Zhao, S. Wang and X. Ma, *Appl. Catal., B*, 2020, **277**, 119278.

35 A. Kambolis, H. Matralis, A. Trovarelli and C. Papadopoulou, *Appl. Catal., A*, 2010, **377**, 16–26.

36 Z. Fei, X. Xie, Y. Dai, H. Liu, X. Chen, J. Tang, M. Cui and X. Qiao, *Ind. Eng. Chem. Res.*, 2014, **53**, 19438–19445.

37 A. Trovarelli, M. Boaro, E. Rocchini, C. de Leitenburg and G. Dolcetti, *J. Alloys Compd.*, 2001, **323**, 584–591.

38 M. Wang, S. Y. Kim, A. Jamsaz, N. Pham-Ngoc, Y. Men, D. H. Jeong and E. W. Shin, *Catal. Today*, 2024, **425**, 114341.

39 D. J. Kim, *J. Am. Ceram. Soc.*, 1989, **72**, 1415–1421.

40 S. Chen, C. Miao, L. Liang and J. Ouyang, *Energy Fuels*, 2022, **36**, 8340–8350.

41 B. Liu, C. Li, G. Zhang, X. Yao, S. S. Chuang and Z. Li, *ACS Catal.*, 2018, **8**, 10446–10456.

42 J. Ashok, M. Ang and S. Kawi, *Catal. Today*, 2017, **281**, 304–311.

43 Y.-M. Park, S.-H. Chung, H. J. Eom, J.-S. Lee and K.-Y. Lee, *Bioresour. Technol.*, 2010, **101**, 6589–6593.

44 F.-m. Sun, C.-f. Yan, C.-q. Guo and S.-l. Huang, *Int. J. Hydrogen Energy*, 2015, **40**, 15985–15993.

45 S. Bhandari, R. Khatun, M. K. Poddar, A. C. Kothari and R. Bal, *Mol. Catal.*, 2022, **528**, 112473.

46 M. Yi, Y. Zhang, J. Xu, D. Deng, Z. Mao, X. Meng, X. Shi and B. Zhao, *Nanomaterials*, 2021, **11**, 2162.

47 C. E. Hori, H. Permana, K. S. Ng, A. Brenner, K. More, K. M. Rahmoeller and D. Belton, *Appl. Catal., B*, 1998, **16**, 105–117.

48 Y. Zheng, K. Li, H. Wang, X. Zhu, Y. Wei, M. Zheng and Y. Wang, *Energy Fuels*, 2016, **30**, 638–647.

49 G.-Q. Xie, J.-Q. Lu, H.-Y. Zheng, X.-J. Liu, M.-F. Luo and X.-N. Li, *J. Alloys Compd.*, 2010, **493**, 169–174.

50 R. S. Pal, S. Rana, S. K. Sharma, R. Khatun, D. Khurana, T. S. Khan, M. K. Poddar, R. Sharma and R. Bal, *Chem. Eng. J.*, 2023, **458**, 141379.

51 W. Kang and A. Varma, *Appl. Catal., B*, 2018, **220**, 409–416.

52 R. A. El-Salamony, K. Acharya, A. S. Al-Fatesh, A. I. Osman, S. B. Alreshaidan, N. S. Kumar, H. Ahmed and R. Kumar, *Mol. Catal.*, 2023, **547**, 113378.

53 P. Biswas and D. Kunzru, *Int. J. Hydrogen Energy*, 2007, **32**, 969–980.

54 R. Khatun, S. Bhandari, M. K. Poddar, C. Samanta, T. S. Khan, D. Khurana and R. Bal, *Int. J. Hydrogen Energy*, 2022, **47**, 38895–38909.

55 J. Lin, C. Ma, Q. Wang, Y. Xu, G. Ma, J. Wang, H. Wang, C. Dong, C. Zhang and M. Ding, *Appl. Catal., B*, 2019, **243**, 262–272.

56 F. Hu, S. Tong, K. Lu, C.-M. Chen, F.-Y. Su, J. Zhou, Z.-H. Lu, X. Wang, G. Feng and R. Zhang, *J. CO2 Util.*, 2019, **34**, 676–687.

57 A. M. Neris, J. M. Ferreira, M. G. Fonseca and I. M. G. dos Santos, *J. Therm. Anal. Calorim.*, 2021, **143**, 3307–3316.

58 P. E. Quintard, P. Barbéris, A. P. Mirgorodsky and T. Merle-Méjean, *J. Am. Ceram. Soc.*, 2002, **85**, 1745–1749.

59 S. Adak, R. S. Pal, T. S. Khan, M. K. Poddar, M. S. Ahmad, V. V. Prasad, M. A. Haider and R. Bal, *ChemistrySelect*, 2021, **6**, 13051–13059.

60 Z. Wu, M. Li, J. Howe, H. M. Meyer III and S. H. Overbury, *Langmuir*, 2010, **26**, 16595–16606.

61 K. Periyasamy, V. T. Aswathy, M. Manikandan, R. Shukla, A. K. Tyagi and T. Raja, *RSC Adv.*, 2015, **5**, 3619–3626.

62 H. Vidal, J. Kašpar, M. Pijolat, G. Colon, S. Bernal, A. Cordón, V. Perrichon and F. Fally, *Appl. Catal., B*, 2000, **27**, 49–63.

63 R. Wang, S. I. Mutinda and M. Fang, *RSC Adv.*, 2013, **3**, 19508–19514.

64 S. O. Omarov, K. D. Martinson, A. N. Matveyeva, M. I. Chebanenko, V. N. Nevedomskiy and V. I. Popkov, *Fuel Process. Technol.*, 2022, **236**, 107429.

65 J. Xu, R. Xi, Q. Xiao, X. Xu, L. Liu, S. Li, Y. Gong, Z. Zhang, X. Fang and X. Wang, *J. Catal.*, 2022, **408**, 465–477.

66 L. P. Silva, L. E. Terra, A. C. Coutinho and F. B. Passos, *J. Catal.*, 2016, **341**, 1–12.

67 W. Cai, Q. Zhong and W. Zhao, *Chem. Eng. J.*, 2014, **246**, 328–336.

68 X. Wang, Z. Jiang, B. Zheng, Z. Xie and L. Zheng, *CrystEngComm*, 2012, **14**, 7579–7582.

69 W. Shan, M. Fleys, F. Lapicque, D. Swierczynski, A. Kiennemann, Y. Simon and P.-M. Marquaire, *Appl. Catal., A*, 2006, **311**, 24–33.

70 G. Postole, B. Chowdhury, B. Karmakar, K. Pinki, J. Banerji and A. Auroux, *J. Catal.*, 2010, **269**, 110–121.

71 S. K. Sharma, B. Paul, A. Srivastava, R. S. Pal, M. K. Poddar, T. S. Khan, C. Samanta and R. Bal, *Sustain. Chem. Clim. Action*, 2023, **2**, 100019.

72 R.-P. Ye, Q. Li, W. Gong, T. Wang, J. J. Razink, L. Lin, Y.-Y. Qin, Z. Zhou, H. Adidharma and J. Tang, *Appl. Catal., B*, 2020, **268**, 118474.

73 R. S. Pal, S. Rana, S. Sadhu, T. S. Khan, M. K. Poddar, R. K. Singha, S. Sarkar, R. Sharma and R. Bal, *Energy Adv.*, 2023, **2**, 180–197.

74 J. Mei, Y. Shen, Q. Wang, Y. Shen, W. Li, J. Zhao, J. Chen and S. Zhang, *ACS Appl. Mater. Interfaces*, 2022, **14**, 35694–35703.

75 Q. Li, Z. Yan, N. Wang, Z. Xu, G. Wang and G. Huang, *Catal. Sci. Technol.*, 2020, **10**, 4030–4041.

76 Z. Xie, B. Yan, J. H. Lee, Q. Wu, X. Li, B. Zhao, D. Su, L. Zhang and J. G. Chen, *Appl. Catal., B*, 2019, **245**, 376–388.

77 Y. Wang, L. Yao, Y. Wang, S. Wang, Q. Zhao, D. Mao and C. Hu, *ACS Catal.*, 2018, **8**, 6495–6506.

78 M. Wei and X. Shi, *Methane*, 2024, **3**, 86–102.